A circle-based method for detection of neural fibre cross-sections in classically stained 2D electron micrographs

Martin O'Reilly[1,2,3], Arnd Roth[3], Michael Häusser[3] and Lewis D. Griffin[1,2]
[1]CoMPLEX, University College London, London, United Kingdom
[2]Dept. of Computer Science, University College London, London, United Kingdom
[3]Wolfson Institute for Biomedical Research, University College London, London, United Kingdom

***Abstract*— Recent developments in electron microscopy now permit the unambiguous reconstruction of even the smallest neural fibres by human experts. However, manual reconstruction of an interesting volume of neural tissue would take thousands of person-years. Techniques to automate such reconstruction are therefore highly desirable and currently under active development. Here we present a novel circle-based technique and assess its performance on classically stained electron micrographs of the molecular layer of mouse cerebellar cortex. We compare its performance to a recently published pixel-based classifier (ilastik), selected because a similar random forest classifier from the same group has shown promising results on images of neural tissue. The performance of our algorithm and that of ilastik are similar, achieving approximately 50% on an overlap-based f-measure.**

Keywords-basic image features; BIFs; electron microscopy; neural circuit reconstruction; connectomics; ilastik

I. INTRODUCTION

Complete mapping of neural connectivity requires methods for tracing the long-range connections in white matter and methods for reconstructing the local circuitry in grey matter. Local circuit reconstruction necessitates both the accurate tracing of neural fibres and the accurate identification of functional connections between them (synapses). Our interest in this paper concerns automated reconstruction of these local grey matter circuits.

The micro-architecture of grey matter varies between brain areas. Here we focus on the molecular layer of the mouse cerebellum. The circuits within this region are believed to be as complex in their connectivity as any other area, but display a greater degree of global order in their geometry [1]. This order is due to regularities in the orientation of neural fibres. For example, parallel fibres (arising from the ascending axons of granule cells) are all parallel; Purkinje cell dendrites run perpendicular to the parallel fibres and the dendrites of individual Purkinje cells lie flat in the same sagittal plane.

A. Electron microscopy

Reconstruction of grey matter circuitry requires imagery with high, ideally isotropic, resolution. For many years electron microscopy (EM) has achieved sufficient resolution in x and y, but not in z. The recent combination of block-face scanning [2] and focussed ion beam milling [3] (together known as FIB-SEM) has solved this problem and is able to produce image volumes of sufficiently high isotropic resolution. All images used here were acquired using FIB-SEM.

All EM techniques require tissue to be stained, with different stains varying in the structures made visible. *Classical* staining reveals a sufficient range of structures to allow accurate manual tracing of fibres and identification of synapses. An alternative *extracellular* stain marks only extracellular space and cell outer membranes. This makes tracing of fibres easier but identification of synapses unreliable in most types of neural tissue (one exception is the retina [4]). Many recent algorithms for automated reconstruction of local circuitry from high-resolution EM imagery have focussed on this extracellular staining. Here we use the more challenging but fully informative classical stain.

Although we use FIB-SEM data, in this initial work we do not take advantage of its isotropic resolution, instead focussing on 2D sagittal slices. Since parallel fibres run orthogonal to the sagittal plane, in most sagittal slices the boundaries of the vast majority of visible fibres appear as dark convex contours, some containing intracellular clutter.

B. Automated reconstruction

While classically stained FIB-SEM imagery permits the accurate manual tracing of fibres and identification of synapses, manual reconstruction of circuits of an interesting size would take thousands of person-years [1]. Therefore automated reconstruction techniques are required.

In this problem, as in many problems in computer vision, a distinction can be drawn between *bottom up* and *top down* approaches. Bottom up approaches construct locally optimal solutions directly from the image data by classification of pixels based on local image neighbourhood [6, 7, 8, 9, 10, 11]. These solutions are fast and simple to compute but do not take into consideration any long-range regularities in the ground truth solutions. The consequence of this is that a bottom up

[1] Based on tracing rates given in [5] we estimate a $1mm^3$ volume of mouse cerebellar cortex would take between 11 and 22 thousand person-years to manually reconstruct.

approach will frequently output highly non-convex boundaries for located structures, even though for the images we are considering the true boundaries are mostly convex.

Long-range regularities can be taken into consideration using top down approaches. The most common top down approaches applied to this problem are variants of the *active contour* method [12, 13, 14]. This attempts to find the set of boundary contours that are well supported by the image data while exhibiting the regularities observed in the ground truth data. Such regularities can include both geometrical constraints (e.g. convexity) and interaction constraints (e.g. limiting overlap between contours). However, unlike the bottom up approach, the optimal solution cannot be directly constructed and must instead be searched for. The solution space of possible sets of contours is too vast to exhaustively evaluate and can only be searched by local refinement. It is likely to contain many local optima and so the quality of the found 'optimal' solution is highly dependent on where the search starts. Thus, while this method is effective for propagating a known good set of contours to an adjacent slice, it is much less effective when a good quality initialisation is unavailable.

We present a top down approach that goes further than the active contour method in its treatment of long-range regularities. Rather than simply encouraging these regularities, as is done in active contour methods, our *circle-based fibre detection algorithm* enforces them. This greatly reduces the size of the solution space and makes finding a near optimum solution computationally feasible. Our approach is to represent neural cross-sections as circular, with a quantised range of possible radii. This reduces the solution space to a finite set of candidate circles at each pixel. It then becomes possible to greedily construct a set of low-overlap circles that are near optimally supported by the data. The near circularity of fibre cross-sections in our data is shown in figure 1.

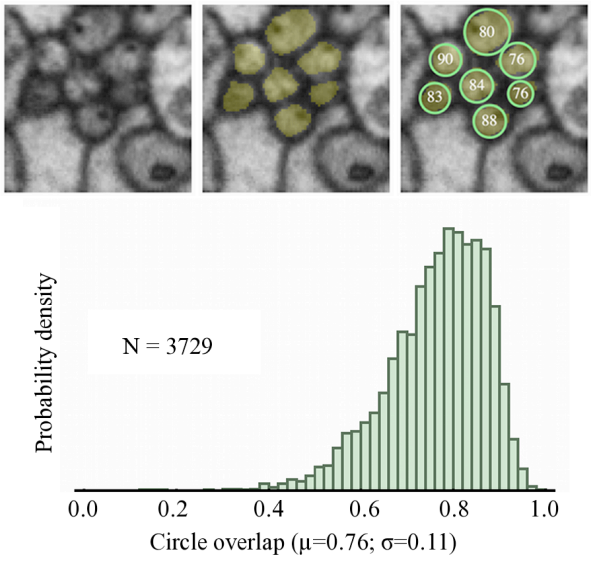

Figure 1. The cross-sections of many fibres are well represented by circles. Top-left: a cluster of fibre cross-sections; Top-middle: their manually traced ground truth; Top-right: the best fitting circles and their percentage overlap with the ground truth; Bottom: the distribution of fitted circle overlap for all fibre cross-sections. The best fitting circle for a ground truth object is that with the same centre of gravity and area. Overlap is a measure of agreement between two shapes and is defined in section II.B

We compare the performance of our circle-based classifier to that of ilastik [15], a recently published pixel-based classifier. Ilastik was chosen because a similar random forest classifier from the same group has shown promising results on images of neural tissue [6].

II. METHODS

A. Data preparation

A sample from the molecular layer of a perfusion-fixed mouse cerebellum was classically stained using a reduced OTO method [16]. The sample was then imaged in sagittal sections using an NVision 40 Focussed Ion Beam Scanning Electron Microscope (FIB-SEM), at an isotropic resolution of 9.3nm. Three sagittal slices from a 2548x852x512 voxel volume were used for this study. These slices were at least 170 voxels (1.6μm) apart to ensure that successive cross-sections of the same fibre were not correlated in shape or size. Each slice was split to produce a total of six half-slices. One half-slice was used for algorithm training, another for parameter tuning and the remaining four were used to generate unbiased estimates of algorithm performance.

All extracellular membrane pixels in these six half-slices were manually labelled using TrakEM2 [17]. The remaining pixels were grouped by a connected component analysis. Each connected component object corresponds to a cross-section through a parallel fibre, a Purkinje cell dendrite, an interneuron fibre or part of a glial cell. We refer to these components as *cells*. Each cell was identified as either *fibre* or *other*. Fibres that abut the border of the half-slice were identified as other. These connected component objects were then expanded by two pixels via morphological dilation to produce two sets of ground truth objects. The *fibre-only* ground truth contains only fibre objects and is used to evaluate our circle-based fibre detection algorithm. The *all-cell* ground truth contains all objects and is used to evaluate ilastik. The use of two different ground truths for the two algorithms is discussed in more detail in section E.

B. Overlap as a measure of similarity

The overlap between two objects is defined as the intersection of the two objects (number of common pixels) divided by their union (number of pixels contained by either object), and is equivalent to the *Jaccard index* (referred to as the *coefficient de communauté* in [18]; and the *coefficient of community* in [19]).

To evaluate the quality of a set of algorithm-generated objects we make use of the overlap measure in a multi-step process. The first step is to calculate a list of *candidate pairings* comprising all pairings, with a non-zero overlap, of an algorithm-generated object with a ground truth object. Next, the candidate pairing with the highest overlap is identified and moved to a list of *matched pairings*. All remaining candidate pairings containing one or other member of the matched pair are removed from the candidate list. The process is repeated starting with the identification of the pairing with the highest overlap from the current candidate list. This is continued until

no candidate pairings with non-zero overlap remain. Next, we define the *matched overlap* for ground truth and algorithm-generated objects. If an object occurs in a pairing in the matched list (it cannot occur more than once) then its matched overlap is set to be the overlap of the pairing. All other matched overlaps are set to zero. *Precision* is defined as the mean matched overlap for algorithm-generated objects. *Recall* is defined as the mean matched overlap for ground truth objects. We then take the harmonic mean of precision and recall to get the *f-measure*, a commonly used metric for evaluating the similarity between a set of algorithm-generated objects and a set of ground truth objects. This overlap-based f-measure is equivalent to the *Dice coefficient* (referred to as the *coincidence index* in [20]).

C. *The circle-based fibre detection algorithm*

Our algorithm represents fibre cross-sections as circles. Our set of candidate fibres for an image is therefore the set of circles, centred on pixels and with radii from a discrete set, which are fully contained within the image. We compute a feature vector for each candidate circle (section C.1) and compute, on the basis of it, a 'fibreness' score (section C.2). We then select a subset of candidate circles on the basis of this score and the constraint that fibre circles should have limited overlap (section C.3).

1) *The fibreness feature vector*

Our algorithm makes use of a map of oriented Basic Image Features (oBIFs [21, 22]) computed from the responses of a bank of six 2D derivative-of-Gaussian linear filters. BIFs are a classification of local image structure into seven different classes on the basis of approximate local symmetry. oBIFs augment the BIF with a quantised orientation, the computation of which depends upon the BIF type. Different BIF types have either zero, four or eight possible orientations, giving 23 oBIF types. The computation of BIFs depends on two parameters, a filter scale (σ) and a 'flat' threshold (γ). Figure 2 shows a sample BIF map. For this work we set $\sigma = 1.75$ and $\gamma = 0.085$.

The *fibreness feature vector* for a candidate circle is based on the distribution of oBIFs within an annular region. This region is co-centred with the circle and has inner and outer radii of 0.6 and 1.3 times the circle radius. As our fibre model is circularly symmetric, rather than using absolute orientation, we use a system of quantised, unsigned orientations measured relative to the radius vector from the circle centre to the oBIF location. We call this system of features rBIFs. Maintaining the same precision of orientation quantisation as for the 23 oBIFs results in 17 rBIFs. Figure 2 shows the annular region for a particular candidate circle, along with the distribution of rBIFs within it. For this work we use the mean square-rooted rBIF histogram across 8 overlapping quadrants as our feature vector.

2) *A fibreness score*

For our training half-slice, as well as computing fibreness feature vectors for each candidate circle, we also compute a *fibreness score*. This score measures how consistent the circle is with the ground truth. The score is computed as the maximum overlap between the circle and any of the ground truth fibre objects. We use logistic regression to learn an approximation of the relationship between the fibreness feature vector and the fibreness score.

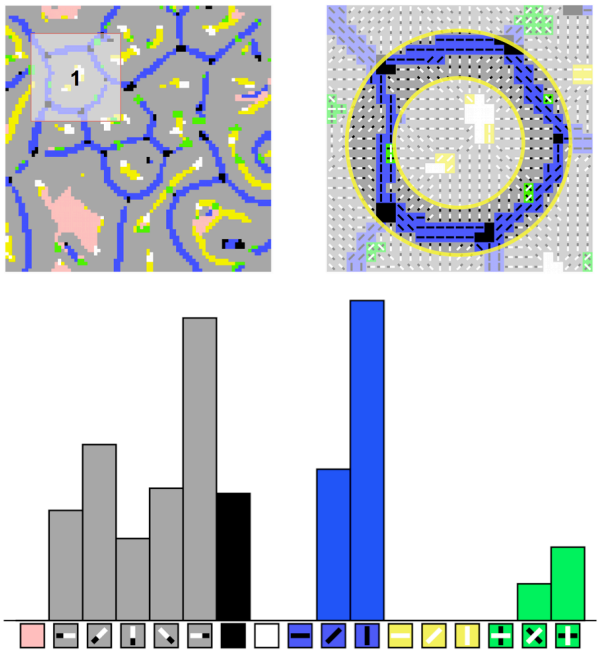

Figure 2. Top-left: the BIF map corresponding to the image region shown in figure 1. Top-right: an expanded view of the area indicated in the top-left image. This shows the annular region associated with a candiate circle overlaid on the oBIF map for the area. Bottom: the distribution of rBIFs within the annular region shown in the top-right image.

To learn this relationship, the fibreness score is computed for all circles, centred on pixels and with integer radii from 6 to 77 pixels, whose annular regions are fully contained within the training half-slice. A two-pass targeted sample is used to select approximately 65,000 training circles from this x, y, r volume. In the first pass, points are picked such that the distribution of radii in the sample matches the distribution of fibre radii in the ground truth. In the second pass, points are picked from this first sample such that the distribution of fibreness scores is uniform. This targeted sample of training points was found to result in much improved fibre-finding performance compared to a random sample.

3) *Fibre finding*

Fibreness feature vectors are calculated for a range of candidate circles, centred on pixels and with a selection of integer radii, whose annular regions are fully contained within the test half-slice. The selected radii are geometrically sampled from the range 6 to 77, with a multiplier of 1.17. The weight vector learned via logistic regression is used to generate a predicted overlap score for every candidate circle from its fibreness feature vector, producing an x, y, r score volume. The global maximum of this score volume is found and the circle associated with this x, y, r is selected as a potential 'found fibre'. If the mean luminance of the image within this circle is above a threshold (24% of maximum intensity) the circle is retained as a confirmed found fibre. Otherwise, the circle is rejected as being wholly within a mitochondrion. If the circle is retained, all other circles that would overlap significantly with the found fibre are excluded from subsequent selection. Circle overlap is deemed significant when one circle would contain the other's centre. The global maximum of remaining non-selected, non-excluded points in the score volume is selected

and the process repeated until a pre-determined minimum predicted fibreness score (65%) is reached. The stopping score and grey level mitochondrion exclusion threshold are set by maximising the overlap-based f-measure achieved against a separate tuning half-slice. Overlap is calculated between the found circles and the fibre-only ground truth objects.

D. The ilastik pixel classifier algorithm

1) The classifier

Ilastik [15] is a recently published pixel-based random forest classifier. A similar classifier has been reported by the same group to perform well at finding cell boundaries in electron microscope images of neural tissue [6]. The version of ilastik used for this study (v0.5) has a range of image features available, including ones based on similar derivative-of-Gaussian filters as those used in the BIF scheme. These features are available at a range of scales, ranging from $\sigma = 0.3$ to $\sigma = 10$. The classifier trained here uses all features at all scales and is trained on the full extra-cellular membrane pixel labelling for the training half-slice. Labelled membrane pixels are assigned to one ilastik class and all unlabelled pixels are assigned to a second class.

At each training iteration, ilastik outputs an estimate of the probability that each pixel is extracellular membrane. This probability estimate is thresholded, assigning pixels with estimated probability ≥ 0.5 to the *membrane* category and the remaining pixels to the *non-membrane* category. During training, ilastik minimises the pixel error between this post-threshold category labelling and the ground truth membrane labelling.

2) Post-processing

The final output of ilastik is an estimate of the probability that each pixel in the test image is extra-cellular membrane. As in [6] this probability map is converted into a set of algorithm-generated objects using the watershed algorithm, using all pixels with a low membrane probability as seeds and removing all segments below a certain size. Additionally, we also independently subject all remaining segments to morphological closing. This fills holes and cracks in segments without merging or splitting any segments. All three post-processing parameters are optimised by maximising the overlap-based f-measure achieved against a separate tuning half-slice. Overlap is calculated between the algorithm-generated objects and the all-cell ground truth objects.

The approach in [6] is to deliberately produce an over-segmentation of *super-voxels* from the watershed stage and train another random forest classifier to merge these super-voxels. This functionality is not available in ilastik. However, we simulated a 'perfect' super-voxel merging algorithm by relaxing the one-to-one matching constraint when scoring the algorithm-generated objects against the ground truth. This has the effect of merging any algorithm-generated objects that maximally overlap with the same ground truth object. However, even after re-tuning the watershed parameters under this relaxed scoring regime, this did not result in a significant improvement in performance. This suggests that the addition of a voxel-merging stage would not result in a significant improvement in the performance of ilastik on our data. This may be due to the fact that not all the features used in [6] are available in ilastik. However, it appears that the tissue used in [6] was prepared using extra-cellular staining. Therefore another possibility is that it is simply not possible to produce a true under-segmentation from the membrane map that can be generated from the more cluttered classical staining.

E. Algorithm comparison

Our algorithm has a different aim than many other algorithms designed to reconstruct neural fibres from electron micrographs. Most 2D algorithms (including ilastik) try to identify all cell parts in the image, producing a dense labelling of pixels. Our algorithm only attempts to find closed 2D fibre cross-sections, producing a sparse labelling of fitted circles. It is not clear what the fairest way to compare these two differing outputs is. It could be argued that the additional objects found by ilastik might be harder to accurately find than the fibres to which the circle-based algorithm limits itself. To determine if this was the case, the recall for the fibre-only ground truth was compared for both algorithms. Recall gives credit for all parts of algorithm-generated objects that overlap the ground truth but does not penalise any parts that do not overlap the ground truth. Using this measure, the relative performance of the two algorithms was much the same as that observed when comparing their f-measure scores evaluated against their different ground truths. This suggests that ilastik does not find non-fibres harder to detect than fibres and that, despite the different ground truths used for evaluation, the algorithms can be fairly compared using their respective f-measures.

III. Results

A. Circle-based algorithm

Figure 3 shows the fibre circles found by our algorithm on one of the test half-slices, along with the fibre-only ground truth objects for the half-slice. Note that many of the circles with zero matched overlap do actually overlap with a true fibre object. However, the algorithm scoring only permits one found circle to be associated with each true fibre, so only the circle that most overlaps with each ground truth fibre will contribute to the f-measure.

The labelling produced by our circle-based algorithm is sparse. The found circles are predominantly constrained to the areas of the image where the ground truth fibres exist, with few circles found in areas where there are no fibres. For the example half-slice shown, only 11% of the found circles (47/442) are placed completely outside of the ground truth fibres, despite this 'non-fibre' area accounting for 66% of the slice.

However, there are many objects that are not well found. 35% (160/455) of true fibres are not well matched by any found circle (i.e. have a matched overlap of less than 50%). The algorithm seems to find most small, round fibres well but struggles to find larger, irregular fibres. It also seems to miss some very small fibres. Many of the fibre cross-sections that are not well found are pre-synaptic boutons (marked B in figure 3). These are points where a fibre swells and makes a synapse and their cross-sections are both large and irregular.

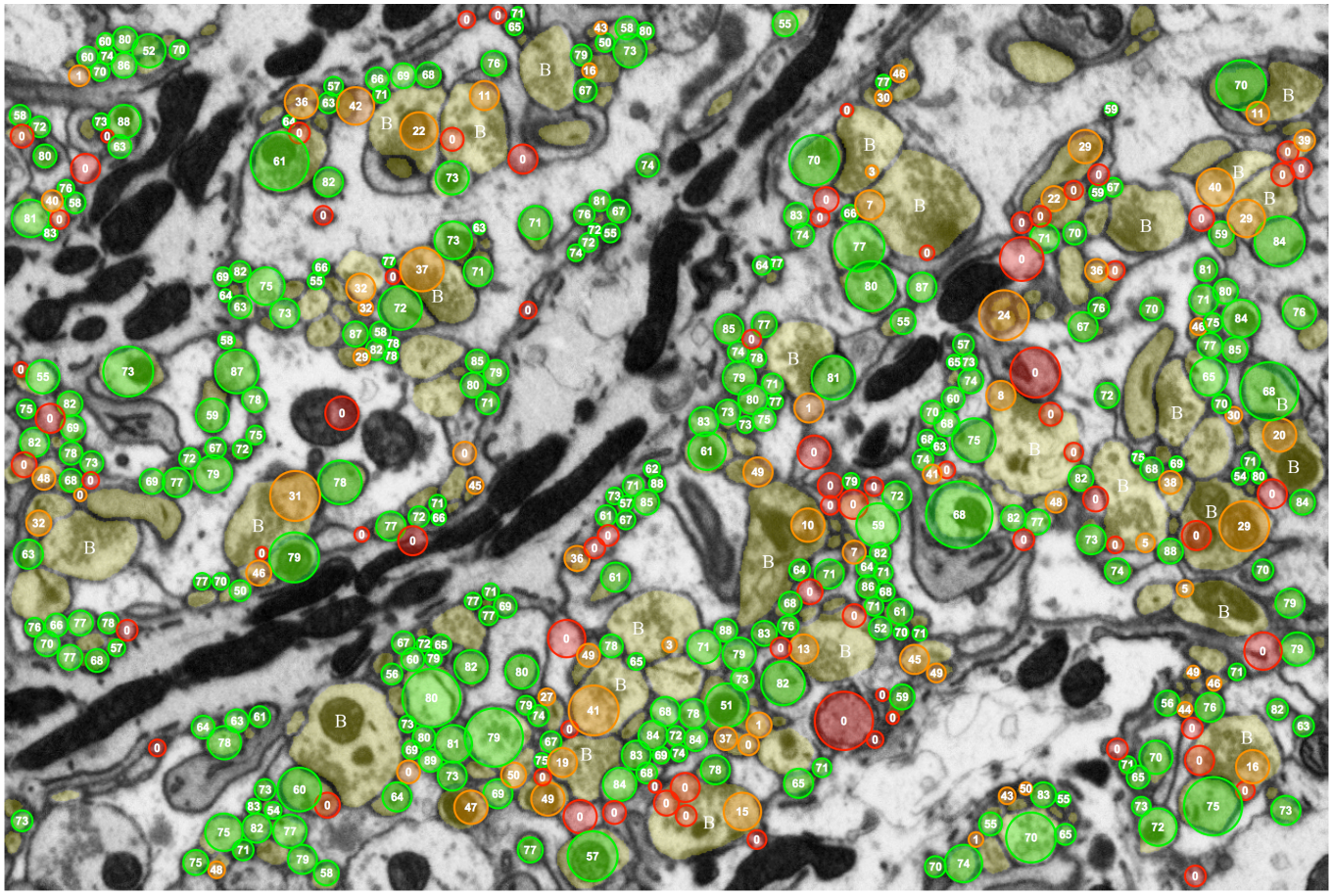

Figure 3. The fibre circles found by our algorithm overlaid on a sample test slice with fibre-only ground truth objects highlighted in yellow. The numbers indicate the percentage matched overlap between the found fibre circle and its paired ground truth object. Each ground truth object can only be paired with one circle, so some circles are assigned a score of zero even though they overlap a ground truth object. Green circles have a high matched overlap (≥50%); orange circles have a low matched overlap (<50%); red circles have a matched overlap of zero. Pre-synaptic boutons are marked with B.

Figure 4 shows how the distribution of overlap scores varies with the size and eccentricity of the true fibres (data pooled across all four test half-slices). The algorithm fails to find fibre cross-sections well if they are very small (<188 pixels), very large (>1397 pixels) or too irregular in shape (eccentricity>1.4). The poor performance on very small and very large fibres remains when only very circular fibres are considered (data not shown).

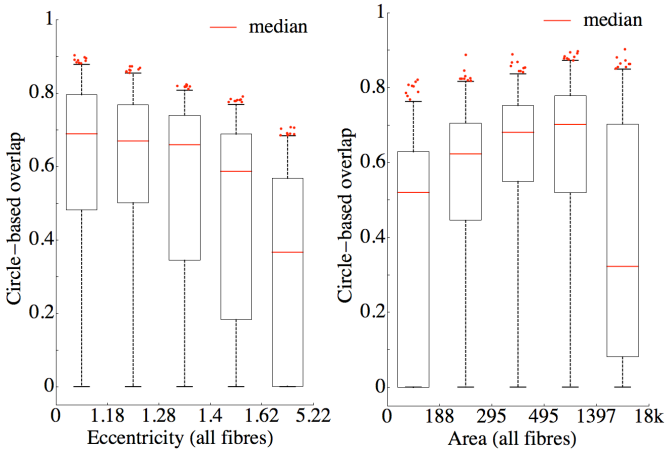

Figure 4: Left: the overlap achieved by our algorithm as a function of the eccentricity of true fibres. Right: the overlap achieved by our algorithm as a function of the area of true fibres. Box bounds indicate 25th and 75th percentiles. Whisker bounds indicate 2.5th and 97.5th percentiles. Note that an equal number of data points contribute to each box-whisker column, resulting in non-uniform x-axes.

B. *Algorithm comparison*

The mean f-measure performance of the circle-based algorithm assessed against the fibre-only ground truth is 50.5 +/- 1.5%[2] with a standard deviation of 0.9%. The mean f-measure for ilastik assessed against the all-cell ground truth is 51.6 +/- 3.7% with a standard deviation of 2.3%. These mean f-measures are very similar and the difference between them is not significant given the confidence intervals.

IV. Discussion

89% of the circles found by the circle-based algorithm overlap the sparse fibre-only ground truth to some extent. In this respect, the algorithm has managed to distinguish areas of fibre from areas of non-fibre reasonably well. Assessed quantitatively via the overlap-based f-measure, the algorithm achieves parity with a random forest classifier of a type that has been shown to achieve promising results against other electron microscope data. This suggests that this approach merits

[2] 95% confidence interval of the mean

further study. Additionally, a comparison of the output of the two algorithms (not shown) reveals that, while many fibres are well found by both algorithms, there are subsets of fibres that are only well found by one algorithm. This suggests that there is a benefit to be gained if a way can be found to usefully combine the two approaches.

In general our algorithm finds high overlap circles for low eccentricity (i.e. close to circular) fibres and fails to find high-overlap circles for more eccentric fibres (figure 4). This suggests that the algorithm does well when the true fibre cross-sections are a good fit for the circular constraint it imposes on found fibres. One obvious step would be to relax the constraint that found fibres be circles. By permitting found fibres to be ellipses, the model fibres would be a better fit for the high eccentricity fibre cross-sections. However, it remains to be shown whether an exhaustive search of the solution space is still possible with this more complex model.

However, eccentricity is not the full story. Even when constrained to highly circular fibres, very small and very large fibres are still not well found (data not shown). The width of the annular region of interest for which the rBIF histogram is calculated is proportional to the radius of the candidate fibre circle. Permitting this relationship to vary for fibres of different radii may improve the performance of the algorithm for small and large fibres.

Many of the large irregular, poorly found fibre cross-sections are pre-synaptic boutons. These contain a significant amount of intracellular clutter in the form of vesicles and mitochondria. The BIFs associated with this clutter are similar to those associated with fibre boundaries, so this clutter may also contribute to the poor match between found circles and boutons. Introducing new image features that permit this clutter to be clearly distinguished from extracellular membrane may therefore improve the algorithm's performance for bouton cross-sections.

Further work is required for both algorithms to determine to what extent performance at detecting 2D fibre cross-sections translates into performance at reconstructing fibres in 3D from these cross-sections. One the one hand, 3D performance might be expected to be worse than 2D as an error in a single slice could assign an entire section of neurite to the wrong neuron. On the other hand, pooling information across slices could result in higher reconstruction fidelity.

ACKNOWLEDGEMENTS

We are grateful to Sarah Rieubland for preparing and imaging the tissue sample and to Rashmi Gamage, Sophie Gordon-Smith and Trisha Patel for creating the manual membrane labelling. Martin O'Reilly is supported by an EPSRC studentship administered by CoMPLEX. We are grateful to the Gatsby Charitable Foundation for supporting this project.

REFERENCES

[1] Palay S.L. & Chan-Palay V. "Cerebellar cortex: cytology and organization". New York: Springer, 1974.

[2] Denk, W. & Horstmann, H. "Serial block-face scanning electron microscopy to reconstruct three-dimensional tissue nanostructure". PLoS Biology, 2, e329, 2004.

[3] Knott, G.; Marchman, H.; Wall, D. & Lich, B. "Serial section scanning electron microscopy of adult brain tissue using focused ion beam milling". Journal of Neuroscience, 28, 2959-2964, 2008.

[4] Briggman K.L.; Helmstaedter M.; Denk W. "Wiring specificity in the direction-selectivity circuit of the retina". Nature, 471,183-188, 2011.

[5] Helmstaedter, M.; Briggman, K.L. & Denk, W. "3D structural imaging of the brain with photons and electrons". Current Opinion in Neurobiology, 18, 633-641, 2008.

[6] Andres, B.; Köthe, U.; Helmstaedter, M.; Denk, W. & Hamprecht, F. "Segmentation of SBFSEM volume data of neural tissue by hierarchical classification". Pattern Recognition (Proceedings of the 30th DAGM Symposium), LNCS 5096, 142-152, 2008.

[7] Venkataraju, K.U.; Paiva, A.R.C.; Jurrus, E. & Tasdizen, T. "Automatic markup of neural cell membranes using boosted decision stumps". Proceedings of the Sixth IEEE Symposium on Biomedical Imaging (ISBI), 1039-1042, 2009.

[8] Chklovskii D.B.; Vitaladevuni S. & Scheffer L.K. "Semi-automated reconstruction of neural circuits using electron microscopy". Current Opinion in Neurobiology, 20(5), 667-675, 2010.

[9] Mishchenko, Y. "Automation of 3D reconstruction of neural tissue from large volume of conventional serial section transmission electron micrographs". Journal of Neuroscience Methods, 176, 276-289, 2009.

[10] Jain, V. et al. "Boundary learning by optimization with topological constraints". IEEE Conference on Computer Vision and Pattern Recognition (CVPR), 2010.

[11] Turaga, S.C. et al. "Convolutional networks can learn to generate affinity graphs for image segmentation". Neural Computation, 22, 511-538, 2010.

[12] Jurrus, E. et al. "Axon tracking in serial block-face scanning electron microscopy". Medical Image Analysis, 13, 180-188, 2009.

[13] Vazquez-Reina, A.; Miller, E. & Pfister, H. "Multiphase geometric couplings for the segmentation of neural processes". IEEE Conference on Computer Vision and Pattern Recognition (CVPR), 2020-2027, 2009.

[14] Macke, J. H.; Maack, N.; Gupta, R.; Denk, W.; Schölkopf, B. & Borst, A. "Contour-propagation algorithms for semi-automated reconstruction of neural processes". Journal of Neuroscience Methods, 167, 349-357, 2008.

[15] Sommer, C.; Straehle, C.; Koethe, U. & Hamprecht, F.A. "ilastik: interactive learning and segmentation toolkit". 8th IEEE International Symposium on Biomedical Imaging (ISBI), 2011.

[16] Willingham, M.C. & Rutherford, A.V. "The use of osmium-thiocarbohydrazide-osmium (OTO) and ferrocyanide-reduced osmium methods to enhance membrane contrast and preservation in cultured cells". Journal of Histochemistry and Cytochemistry, 32, 455, 1984.

[17] Cardona, A. et al. "An integrated micro- and macroarchitectural analysis of the Drosophila brain by computer-assisted serial section electron microscopy". PLoS Biology, 8, e1000502, 2010.

[18] Jaccard, P. "Distribution de la flore alpine dans le Bassin des Drouces et dans quelques regions voisines". Bulletin de la Société vaudoise des sciences naturelles, 37, 241-272, 1901.

[19] Jaccard, P. "The distribution of the flora in the Alpine zone". New Phytologist, 11, 37-50, 1912.

[20] Dice, L.R. "Measures of the amount of ecologic association between species". Ecology, 26(3), 297-302, 1945.

[21] Crosier M & Griffin L.D. "Using basic image features for texture classification". International Journal of Computer Vision, 88(3), 447-460, 2010.

[22] Lillholm, M. & Griffin, L.D. "Novel image feature alphabets for object recognition". 19th International Conference on Pattern Recognition (ICPR), 1-4, 2008.